Postprint of: Ducka, A., Błaszczak, P., Zajac, M., Maximenko, A., Gazda, M., & Bochentyn, B. (2025). Investigation of the phase transition to the Ruddlesden–Popper phase in La- or Nb-doped Sr2Fe1.5Mo0.5O6−δ double perovskites and the impact of lanthanum or niobium doping. NANOSCALE. https://doi.org/10.1039/d5nr00596e

Investigation of the phase transition to the Ruddlesden-Popper phase in La- or Nb-doped $Sr_2Fe_{1.5}Mo_{0.5}O_{6-\delta}$ double perovskites. Impact of lanthanum or niobium doping

Agata Ducka[(a)*], Patryk Błaszczak[(a,b)], Marcin Zając[(c)], Alexey Maximenko[(c)], Maria Gazda[(a)], Beata Bochentyn[(a)]

[(a)] Faculty of Applied Physics and Mathematics, Gdansk University of Technology, ul. Narutowicza 11/12, 80-233 Gdańsk, Poland

[(b)] Faculty of Electrical and Control Engineering, Gdansk University of Technology, ul. Narutowicza 11/12, 80-233 Gdańsk, Poland

[(c)] National Synchrotron Radiation Centre SOLARIS, Jagiellonian University, Czerwone Maki 98, 30-392 Kraków, Poland

*Corresponding author: agata.ducka@pg.edu.pl

Abstract

$Sr_2Fe_{1.5}Mo_{0.5}O_{6-\delta}$ (SFM) is a well-known representative of a double perovskite family, recognized for its remarkable properties, such as good conductivity in air and hydrogen. However, this material can undergo a phase transition under reductive atmospheres, which might be a challenge for practical use. Herein, we focus on the impact of lanthanum or niobium dopants, which would not only stabilize the structure during the reduction but also have a beneficial impact on the properties of the material, e.g. electrical conductivity. As a result, lanthanum doping (LSFM – $La_{0.3}Sr_{1.7}Fe_{1.5}Mo_{0.5}O_{6-\delta}$) was found to be the most stable and the least new Ruddlesden-Popper phase was formed during the reduction. Moreover, the aliovalent La-doping resulted in increased electrical conductivities in both air and hydrogen, compared to those of pristine SFM. Niobium doping resulted in a behavior similar to that of SFM, with only little stabilization, but the exsolution process in this material was found to be more intense. In situ studies during oxidation allowed us to retrieve the original structure at 700 ° C. Ex-situ XAS analyzes enabled us to focus on the electronic state, which in most cases was restored almost to the original state after the re-oxidation process. This showed that not only the crystallographic structure has been reestablished, but also the local atomic structure. The use of wavelet transform on Fe K-edge allowed us to differentiate contributions from Fe-Fe and Fe-Mo bonds in LSFM.

Keywords: $Sr_2Fe_{1.5}Mo_{0.5}O_{6-\delta}$, double perovskite, Ruddlesden-Popper perovskite, phase transition, doping

Abbreviations and notation:

10Dq – Crystal Field Splitting Parameter (eV)

DC4W – Direct Current-4 Wire Method for Electrical Measurements

DOS – Density of States

DSC – Differential Scanning Calorimetry

E_A – Activation Anergy (eV)

EXAFS – Extended X-ray Absorption Fine Structure

HT-XRD – High Temperature X-ray Diffraction

LSFM - $La_{0.3}Sr_{1.7}Fe_{1.5}Mo_{0.5}O_{6-\delta}$

SFMNb - $Sr_2Fe_{1.425}Mo_{0.475}Nb_{0.1}O_{6-\delta}$

SOC – Solid Oxide Cell

SOFC – Solid Oxide Fuel Cell

sSOFC – symmetrical Solid Oxide Fuel Cell

TEY – Total Electron Yield

TPB – Triple Phase Boundary

TG - Thermogravimetry

YSZ – Yttria Stabilized Zirconia

Ni-YSZ – Nickel Cermet – composite of Ni and YSZ

NPs - Nanoparticles

RP – Ruddlesden-Popper (phase)

SEM – Scanning Electron Microscopy

SFM – $Sr_2Fe_{1.5}Mo_{0.5}O_{6-\delta}$

XANES – X-ray Absorption Near-Edge Spectroscopy

XAS – X-ray Absorption Spectroscopy

XRD – X-ray Diffraction

σ – Electrical Conductivity (S cm^{-1})

1. Introduction

One of the challenges that the world needs to face today is the transition from fossil fuels to renewable energy sources. Additionally, hydrogen technologies are gaining more interest as a way to generate electricity or are used for energy storage. Among them, one may find the Solid Oxide Fuel Cells (SOFCs), which can produce electricity from the chemical energy of the fuel. To make SOFCs even more advantageous, their ability to use fuels other than hydrogen should be developed. Unfortunately, the state-of-the-art anode material, Ni-YSZ cermet, performs poorly under other fuels and is prone to deactivation and carbon agglomeration. Thus, there is a need to develop novel anode materials, that would withstand such conditions. One of the candidates is perovskites with general formula ABO_3, which offers a wide range of potential compounds with different properties [1]. In the perovskite family, double perovskites with the $A_2B_2O_6$ formula can also be identified. Double perovskite can be present in A- or B-site ordered structures, resulting in formulas $AA'B_2O_6$ or $A_2BB'O_6$, respectively. Moreover, different placements of A or B cations can lead to the formation of layered, columnar, or rock-salt ordered structures [1] with the last being the most common [2]. $Sr_2Fe_{1.5}Mo_{0.5}O_{6-\delta}$ (SFM) is one of the representatives of the double perovskite subgroup, which exhibits good redox stability [2–7]. However, in highly reductive atmospheres, SFM compounds may undergo a phase transition to layered perovskite, more specifically the Ruddlesden-Popper (RP) phase $Sr_3Fe_{1.5}Mo_{0.5}O_{7-\delta}$ [8–14]. The RP-phase consists of at least one layer of ABO_3 perovskite structure separated by AO rock-salt layers [10,15]. The Ruddlesden-Popper phases of higher order (more than 1 perovskite slab) are rich in oxygen vacancies in the perovskite layer [15]. Qiu *et al.* [13], Lv *et al.* [16], and Yang *et al.* [17] have shown that despite the formation of the Ruddlesden-Popper phase under hydrogen atmosphere, SFM-based compounds transform back to double perovskite after the reoxidation process. In addition to inconsistency with respect to redox stability, SFM is also characterized by high conductivity in air and hydrogen, making it an interesting candidate for electrodes in sSOFC (symmetrical Solid Oxide Fuel Cells) [4,5,18–21]. Although studies agree that the electrical conductivity of SFM is high, the values reported in the literature vary significantly. Liu *et al.* [20] have obtained extraordinarily high conductivities of 310 S cm^{-1} and 550 S cm^{-1} at 780 °C in hydrogen and air, respectively. Furthermore, Li *et al.* [3] have reported a high conductivity of 116 S cm^{-1} in air. Although these results are undoubtedly impressive, they remain a minority. Most studies [5,19,22–24] present conductivities in the range 10-50 S cm^{-1} in both the mentioned atmospheres and in CO/CO_2 mixtures.

Generally, doping is a standard method for enhancing the properties of any perovskite. Many works are devoted to transition metal-doping at B-site to enhance the catalytic properties of SFM [16,25–29]. Furthermore, electrical conductivity could be increased simultaneously by doping of Ca^{2+}, Ba^{2+}, or La^{3+} at the Sr site [15,25–28].

This work focuses on the doping of SFM with La^{3+} (at the A-site) or Nb^{5+} (at the B-site). In a similar system, Nb-doping for Mo-site was studied and revealed that more oxygen vacancies were formed upon doping [29]. Gou et al. [30] suggested that Nb^{5+} may increase the stability of SFM-based compounds. In their work they have also shown that Nb-doping improves the electrical conductivity in

both air and hydrogen, and finally increases the power density of a symmetrical cell at 800 °C from 374.1 mW cm^{-2} to 531.5 mW cm^{-2}. Yang *et al.* [25] examined the influence of La doping and it was shown that moderate doping enhanced electrical conductivity, but on the other hand, excess La resulted in a decrease in conductivity. Such behavior was explained by an increase in the concentration of anti-site defects and electron density at the Fermi level. Herein, we present a study of the properties of La- or Nb-doped SFM. The impact of the dopant on the phase stability in hydrogen was addressed and extensively studied by various techniques, i.e. high-temperature XRD (X-ray Diffractometry), DSC/TG (Differential Scanning Calorimetry/Thermogravimetry), and several XAS (X-ray Absorption Spectroscopy) measurements. Moreover, the reversible nature of the phase transition was investigated. After the reduction in hydrogen, the exsolution process was observed.

2. Experimental

2.1. Synthesis

The chemical formulas of the prepared materials are as follows: $Sr_2Fe_{1.5}Mo_{0.5}O_{6-\delta}$ (SFM), $La_{0.3}Sr_{1.7}Fe_{1.5}Mo_{0.5}O_{6-\delta}$ (LSFM), and $Sr_2Fe_{1.425}Mo_{0.475}Nb_{0.1}O_{6-\delta}$ (SFMNb). All compounds were synthesized by the modified Pechini method. The appropriate amount of salts ($Fe(NO_3)_3 \cdot 9\ H_2O$, $Sr(NO_3)_2$, and $(NH_4)_6Mo_7O_{24} \cdot 4\ H_2O$) were dissolved in deionized water at room temperature. For doped samples $La(NO_3)_3 \cdot 9\ H_2O$ and $NbCl_5$ were used as source of lanthanum and niobium, respectively. Then citric acid and ethylene glycol were added to the beakers. All reagents used for the synthesis were of analytical grade. The solutions obtained were stirred and gradually heated to 200 °C until gels formed. The gels obtained were transferred to alumina crucibles and fired at 1100 °C for 10 h. The heating and cooling rate was 3 °C min^{-1}. To analyze the stability of the material in the reductive atmosphere and to perform the exsolution, finely ground powders were placed in the tube furnace and reduced under hydrogen flow for 4 h at 800 °C. The part of the reduced powders was re-oxidized in air for 4 h at 800 °C to analyze the reversibility of the phase transition.

2.2. Characterization methods

To determine the phase composition of the materials, X-ray diffraction (XRD) measurements were performed, using Bruker D2 PHASER XE-T. XRD patterns were collected mainly at room temperature, unless otherwise indicated. High-temperature XRD measurements under air atmosphere were performed on a Philipps X'Pert Pro diffractometer with the high-temperature Anthon Paar HT-1200 oven adapter. Both diffractometers are equipped with Cu-Kα radiation sources. To analyze the obtained diffraction patterns, HighScore Plus 3.0.2 software from PANalytican was used.

The microstructure and morphology of the investigated materials were studied using the Scanning Electron Microscope (FEI Quanta FEG 250) with a secondary electron detector operating in high vacuum mode with an acceleration voltage of 10 kV.

Simultaneous thermogravimetry (TG) and differential scanning calorimetry (DSC) measurements were performed under synthetic air on the Netzsch STA 449 F1 Jupiter apparatus. Data were collected from room temperature up to 900 °C at a heating rate of 5 °C min^{-1}. For each analysis, around 10 mg of a powder with ±10% tolerance factor.

X-ray absorption spectroscopy (XAS) measurements were performed at the SOLARIS National Synchrotron Radiation Center in Kraków (Poland) at the PIRX and ASTRA beamlines. For the measurements of the O K-edges and Fe $L_{3,2}$-edges, well-ground powders were evenly distributed on the carbon tape and then placed on the standard flag-style sample holder. The measurements were performed at room temperature under ultra-high vacuum using total electron yield (TEY) mode at the PIRX beamline. The Fe K- and Mo L_3 edges were collected at the ASTRA beamline. The spectra were

measured using a photon beam delivered by a double-bend achromatic 1.3 T bending magnet with a critical energy around 2 keV. For the iron K-edge of the iron, the appropriate amount of finely ground powder was mixed with ethylcellulose (50 μm, Pol-Aura) and pressed into thin pellets. The Fe K-edges were collected at room temperature under ambient pressure and a Ge (220) monochromator was used. At the same time, Fe foil was studied each time as a reference. To measure the Mo L_3-edge, the powders were evenly distributed on a sulfur-free Kapton foil and measured at around 30 Torr. The MoO_3 spectrum was collected every two samples as a reference material and the Si (111) crystal was used as a monochromator. Data were analyzed using the freeware Demeter package. For the Fourier transform EXAFS analysis, the wave vector *k* was considered in the range 2.9 –8.5 $Å^{-1}$ and the phase correction was applied. Because of the complex structure and the overlap of Fe-Fe and Fe-Mo bonds in the radial distribution function, the wavelet analysis was applied to differentiate between them. Wavelet analysis was performed in the Fastosh freeware software. For the analysis η=7.5 and σ=0.5 were used as parameters for the Morlet wavelet transform.

The conductivity of the compounds was measured using the direct current 4-wire method (DC4W). For this purpose, the samples were pressed into square pellets and sintered at 1400 °C for 10 h for densification. Subsequently, dense (>95% relative density) pellets were cut into narrow, rectangular bars, onto which platinum paste (ESL) was brush-painted and Pt wires were attached. For the measurements, Keithley 2401 was used as a current source, while voltage was measured using a Keysight 34970A meter. Each sample was first heated to 800 °C in air, then the conductivity measurements were taken every 50 °C during cooling to 300 °C. After each temperature change, the samples were stabilized for the required amount of time. Before the atmosphere was changed to hydrogen, the cell was rinsed with Ar until no air remained inside, and then the procedure was repeated in hydrogen. The only difference was that the samples were kept at 800 °C for 4 hours to mimic the reduction process.

3. Results and discussion

a. Phase composition and structure of the materials

The diffraction studies revealed that all synthesized compounds were double perovskites in the *Fm-3m* structure, as presented in the XRD diffraction patterns in Fig. 1. For the doped compounds, a slight amount of $SrMoO_4$ can be found, however, based on the Rietveld refinement it was estimated that the samples contained less than 2 wt.% Mo-rich impurities. The presence of SrMoO4 in as-prepared compounds is commonly reported in the literature [29,31–36] and tends to vanish after reduction. The detailed results of the Rietveld refinement may be found in the Tab. 1, while exemplary results of the refinement are presented in Fig.S1 in the Supplementary Materials. Both doped materials have a unit cell larger than that of a pristine strontium ferrite. Although La^{3+} has smaller ionic radii than Sr^{2+}, aliovalent doping may lead to changes in the valence state of Fe or Mo to preserve the electroneutrality of the compound. Both Fe and Mo, when in lower oxidation states, have larger ionic radii than their higher valence counterparts [31] leading to the expansion of the unit cell [32]. Yang *et al.* [25] also explained the expansion of the unit cell upon La-doping by the domination of the electronic effect of La^{3+} over the ionic size. They proposed that an additional electron from La^{3+} influences primarily the Mo valence state, with only little impact on the Fe state [25]. The expansion of the unit cell in the SFMNb material can be directly explained by the size effect. Because niobium is a transition metal close to Mo in the periodic table, it is almost certain that it will incorporate into the B site of the double perovskite, as was aimed during the synthesis. Furthermore, the size of the Nb^{5+} ions is quite similar to that of Fe and Mo ones, and almost twice smaller than Sr^{2+}, thus it was assumed that Nb occupies only B-site of double perovskite. Nb^{5+} cations have an ionic radius equal to 0.64 Å, which is greater than for both possible molybdenum ions (Mo^{5+} 0.61 Å and Mo^{6+} 0.59 Å). At the same time, the

Nb ionic radius is slightly smaller than Fe^{3+} (0.645 Å) and much smaller than Fe^{2+} (0.78 Å) [31]. According to [30], the niobium doping may result in the formation of a higher share of Fe^{2+}, which would lead to cell enlargement.

As evidenced by the formation of a diffraction reflection at ~31 °, after the reduction at 800 °C, the phase transition to the layered perovskite occurred. On the basis of the intensity ratio of the two components of the double reflection around 31-32 °, it can be said that the transition is not complete and some double perovskite residuals remain in the materials. Because the reflection characteristic of the layered perovskite is rather low intensity in La-doped perovskite, it was suggested that lanthanum doping may stabilize the structure and restrict the phase transition. Phase composition was calculated from Rietveld refinement and fitting double perovskite structure ($Sr_2Fe_{1.5}Mo_{0.5}O_{6-\delta}$-*Fm-3m*), oxygen-deficient Ruddlesden-Popper layered perovskite ($Sr_3Fe_{1.5}Mo_{0.5}O_{7-\delta}$ -*I4/mmm*) and iron (*Im-3m*) which can be exsolved from the lattice. The results of the refinement are presented in the Tab. 1. For both the pristine and the Nb-doped samples, the content of newly formed layered perovskite is between 70-80 wt.%, while for the LSFM this amount is about 40 wt.%. Although the presence of the Ruddlesden-Popper phase may be beneficial and enhance the exsolution of catalytically active centers [13,16,33], it also presents several challenges that need to be addressed. As seen in Tab. 1, the double perovskite has a larger unit cell volume compared to the Ruddlesden-Popper phase. Therefore, during reduction, this volume change would introduce significant strain. For potential use as an electrode in SOCs, this may lead to delamination of the electrode and decrease in the TPB (triple phase boundary). Several studies claim that pristine SFM should be redox stable at high temperatures and not susceptible to exsolution phenomena [3,16,34], however, the XRD patterns of the reduced samples revealed the formation of metallic iron. A similar observation was made by Qiu *et al.* [13], for Co-doped SFM. Interestingly, the amount of exsolved iron was the highest (~13 wt.%) for the SFMNb sample, suggesting that Nb-doping at the B-site enhanced the exsolution of iron. Although the segregation energy of Fe (0.91 eV) makes it unfavorable for exsolution, the addition of other transition metals would introduce cation defects and/or oxygen vacancies [16]. As a result, the segregation energy will be lowered, promoting the formation of nanoparticles.

The reversibility of the phase transition was studied after re-oxidizing the materials at 800 °C for 4 h. All compounds were transformed back to their original double perovskite structure without traces of the layered perovskite. Also, in all XRD patterns $SrMoO_4$ was found, even for SFM, which was free of this impurity before reduction. Although the structure was successfully restored, the unit cell was larger than that for as-prepared samples. This relates mostly to pristine and Nb-doped samples, while the La-doped one is characterized by only a slight volume expansion.

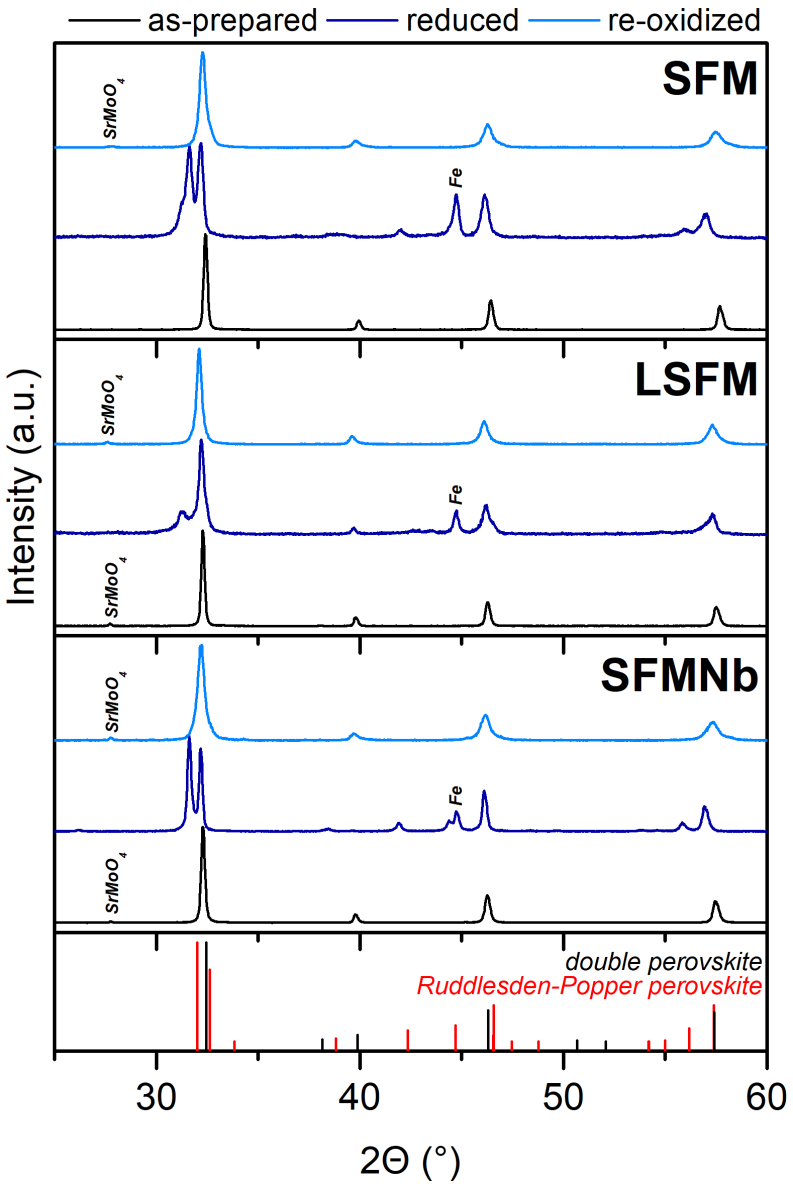

Fig. 1. The XRD patterns of pristine, La-, and Nb-doped SFM in three different states: as-prepared, reduced, and re-oxidized.

Tab. 1. Results of the Rietveld refinement for pristine, La-, and Nb-doped SFM compounds.

			SFM	LSFM	SFMNb
As-prepared	Double perovskite (*Fm-3m*)	a=b=c (Å)	7.8411(2)	7.8533(2)	7.8632(2)
		V (Å^3)	482.09	484.34	486.18
	$SrMoO_4$ amount (wt.%)		n/a	1.7	0.8
	GOF		1.53	1.47	1.65

Reduced	Double perovskite (*Fm-3m*)	a=b=c (Å)	7.854(2)	7.884(1)	7.896(1)
		V(Å^3)	484.49	490.05	492.29
		Amount (wt.%)	17.7	52.2	7.6
	Ruddlesden-Popper layered perovskite (*I4/mmm*)	a=b (Å)	3.9348(6)	3.933(1)	3.9436(2)
		c (Å)	20.361(4)	20.951(9)	20.435(1)
		V(Å^3)	315.24	324.08	317.81
		Amount (wt.%)	73.2	39.2	79.1
	Iron amount (wt.%)		9.1	8.6	13.3
	GOF		2.69	1.67	2.21
As-prepared	Double perovskite (*Fm-3m*)	a=b=c (Å)	7.8516(6)	7.8538(3)	7.8771(6)
		V (Å^3)	484.03	484.44	488.76
	Amount of $SrMoO_4$ (wt.%)		1.2	1.7	1.2
	GOF		1.87	1.55	1.83

SEM images of the as-prepared materials are presented in Fig. S2 in Supplementary Materials. In the case of pristine SFM and SFMNb compounds, the grains' boundaries are obliterated and difficult to spot. On the other hand, La-doping resulted in the formation of well-defined, round-shaped grains. The microstructure of the reduced powders is presented in Fig. 2. Interestingly, the microstructure of the undoped sample seems denser than before the reduction. Although the grains' boundaries are still quite blurred, areas consisting of smaller grains of rectangular shape along the original round grains may be noticed. The existence of the rectangular shape originates from the transition to layered perovskite. Some nanoparticles were found, however, their number is rather low. A similar number of nanoparticles with diameter <100 nm was observed for LSFM. The highest concentration of exsolved NPs was observed for the Nb-doped material, which was expected in the XRD studies showing the highest Fe content. The NPs have a round shape and their diameter is smaller than 100 nm. Enhancement of the exsolution phenomena, thanks to Nb-doping, may result from a lower valence state of Fe ions in the as-prepared compound. Such an observation was reported by Gou *et al.* [30] for similar material. As a result, iron from the lattice is easier reduced on the surface, forming visible nanoparticles. Here, based on [12], in which TEM-EDS did not find any molybdenum in exsolved NPs, it was stated that the formed NPS were composed of metallic Fe, if no other easily reduced transition metal is introduced into the B-site lattice. Although niobium is also a transition metal, its reduction requires much higher temperatures than those used in this experiment [30,35].

The structure of re-oxidized compounds is presented in Fig. S2. Exsolved nanoparticles are not visible anymore after the oxidation, and the microstructure looks a lot like the one of as-prepared materials.

Such an observation indicates the reversibility of the phase transition followed by dissolution of the exsolved NPs. Moreover, it is possible to retrieve not only the specific crystal structure but also the microstructure of the compounds.

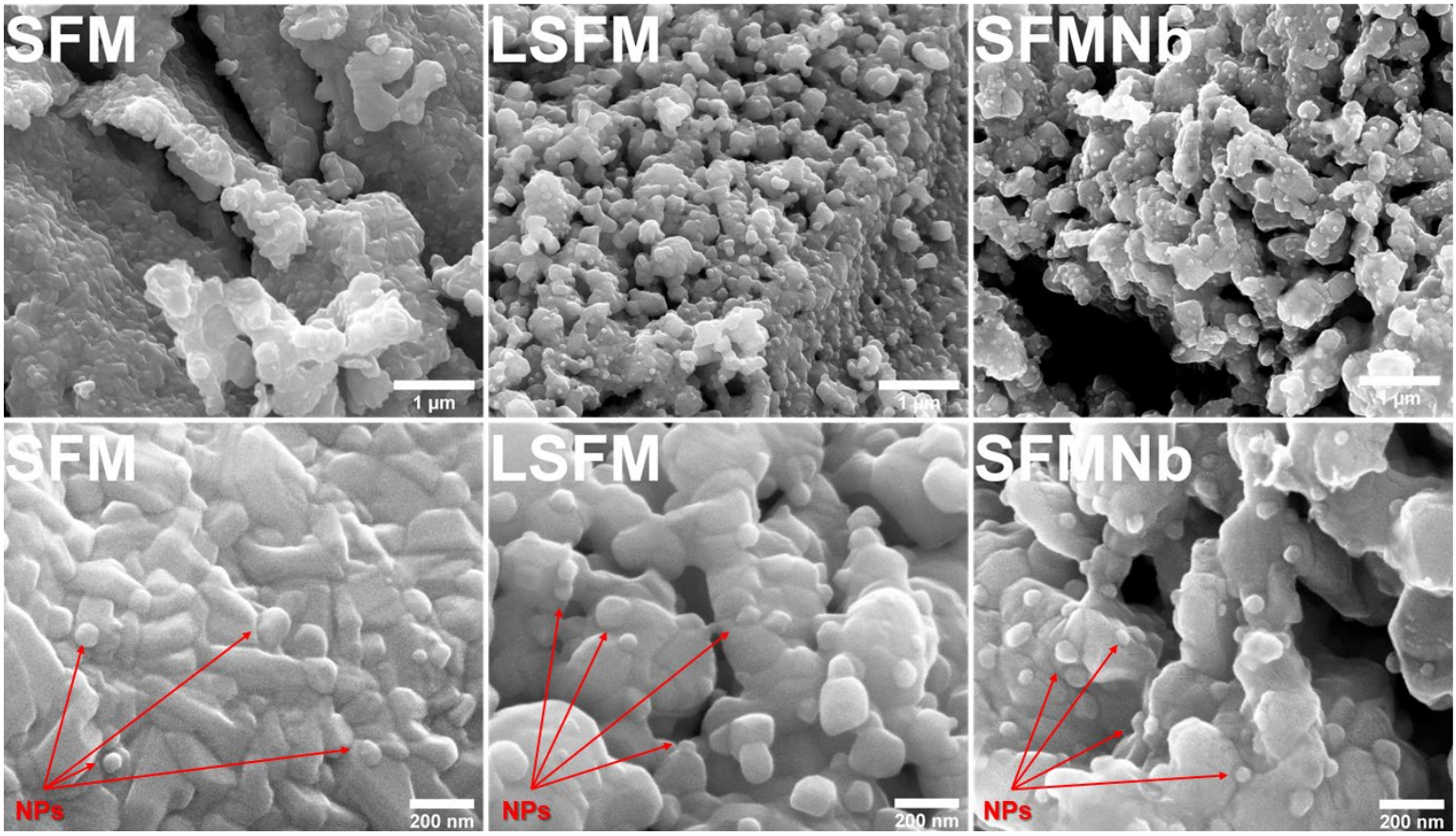

Fig. 2. SEM images of the powders reduced at 800 °C in hydrogen.

b. In-situ oxidation studies from Ruddlesden-Popper to double perovskite

As the phase transition was demonstrated to be reversible by ex-situ XRD analyses, HT-XRD measurements were implemented to investigate the process of shifting from the layered to double perovskite in air. The diffractograms collected during heating are presented in Fig. S3 in the Supplementary Materials. Fig. 3 presents the heat maps of the normalized intensities of the main XRD reflections corresponding to the Ruddlesden-Popper and double perovskite phases vs. temperature. For the pristine and SFMNb samples, the intensities of both reflections between room temperature and approximately 600 °C are comparable, resulting from the highest amount of the RP perovskite. On the other hand, in the case of LSFM, the amount of RP phase is smaller. As a result the diffraction peak at ~31° is less intense and is visible as halo between 31-31.5 °. For all compounds, the reflections shifted towards lower 2Θ, as the unit cells gradually expanded with temperature. At 250 °C, the shift toward higher angles is visible in all three samples, being the most intense for pristine and La-doped SFM. The features seen around 250 °C in Fig. 3 are accompanied by a vanishing signal from iron observed at the same temperature (Fig. S4). This could originate from iron dissolving back into the perovskite and the beginning of the oxidation to the double perovskite. As the temperature was further increased, the main reflections are getting closer to each other, which originates from a decrease in the c-parameter of the Ruddlesden-Popper phase. The peak characteristic of the Ruddlesden-Popper phase vanished between 600 ° C and 700 °C.

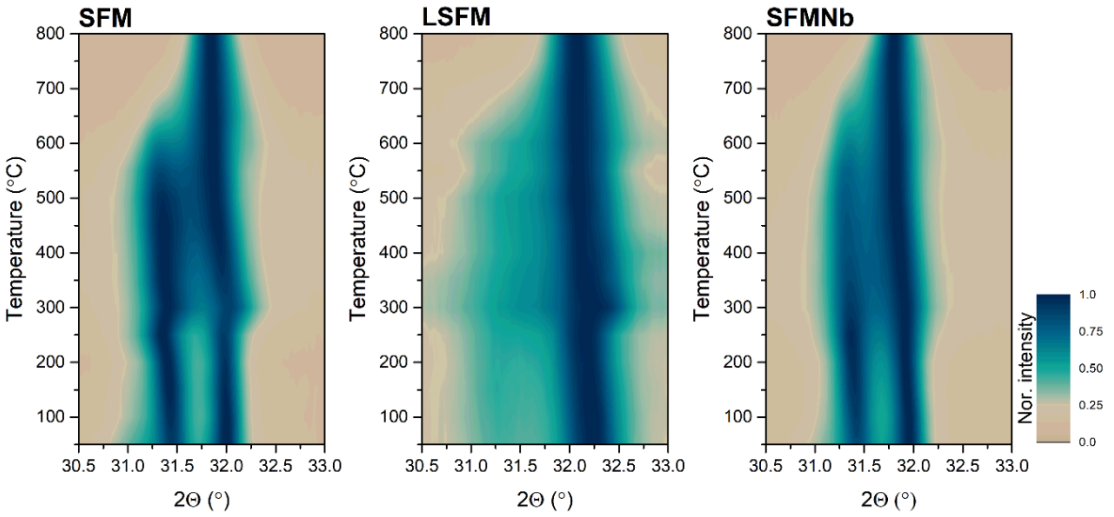

Fig. 3. The heatmaps of the normalized main peak from reduced samples obtained from in-situ oxidation studies.

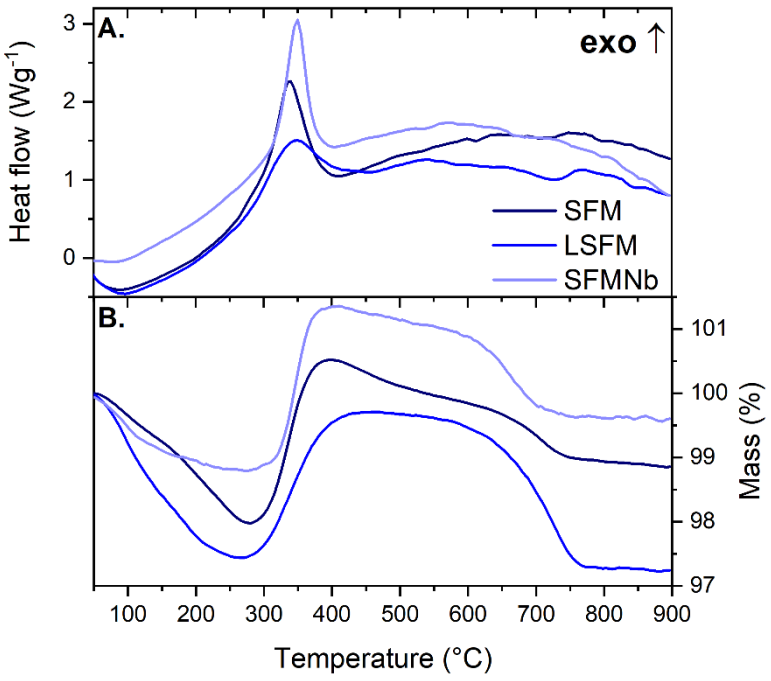

Fig. 4. Simultaneous thermal analyses for re-oxidation of pristine, La-, and Nb-doped SFM compounds: A. DSC and B. TG.

To further analyze the phase transition, DSC/TG measurements were performed on the pre-reduced powders. The results are shown in **Fig. 4**. The first process, clearly seen on the TG curve up to 200 °C results from a release of adsorbed water. Further, a slower decrease in mass (between 200 and 300 °C) may be due to the loss of structural water. With further increase in temperature, the mass above 300 °C increases at a higher rate for SFM and SFMNb, while for LSFM the process is more gradual. In addition, the increase in the TG signal correlates with an exothermic DSC peak, which originates from the oxidation of iron. The temperature of the process corresponds well with the vanishing of the iron peak in HT-XRD (Fig.S4). Furthermore, the intensity of the DSC peak is the highest for the SFMNb sample, which was characterized by the highest amount of exsolved Fe nanoparticles, presented in both XRD and SEM analyses. In the DSC signal, no other clearly distinguishable peaks were found. However, the TG signal shows a gradual loss of mass, except for the LSFM sample, in the 350-650 °C range, which perfectly fits the phase transition regime visible in HT-XRD. The mass drops above 700 °C (750 °C for LSFM), which is likely the result of the release of surplus oxygen from the Ruddlesden-Popper phase. The combined mass loss at 750 °C and the

formation of a single peak in HT-XRD are indicators of complete phase transition to double perovskite.

c. Ex-situ X-ray absorption studies

The O-K edge spectra collected for pristine, La- and Nb-doped SFM in three different states are presented in Figs. 5A-C. The peaks visible in the spectra can be assigned to the respective excitation of O 1s: to the hybridized Fe 3d - O 2p (~530 eV), followed by Sr 4d – O 2p (~536 eV) and Fe 4sp- O 2p (~543 eV) [36–38]. Iron in perovskites is predominantly present in the $3d^5$ ground state. Abbate *et al.* [37] have studied ground states in both $SrFeO_3$ and $LaFeO_3$. They concluded that in $SrFeO_3$ iron is found in the $3d^5\underline{L}$ (Fe^{4+}) state, where L stands for the presence of ligand holes, while for $LaFeO_3$ the iron ground state is $3d^5$ (Fe^{3+}). Here, the presence of the Fe^{4+} $3d^5\underline{L}$ state can be recognized by the pre-peak feature at ~528 eV, which is most intense for re-oxidized SFM and LSFM. The as-prepared samples are also characterized by this feature, but with a lower intensity. The main peak visible for all spectra of the prepared sample originating from the t_{2g} orbital is slightly shifted to lower energies when compared to the signal for Fe^{3+} oxides, also the presence of Fe^{4+} in these states [37,39]. On the other hand, the signal from higher e_g orbitals is visible only as a small bump around 534 eV. Xi *et al.*[40] have explained the enhanced formation of the e_g orbitals by the structural deformation. The formation of the t_{2g} and e_g peaks originates from crystal field splitting around the transition metal sites [38,40].

After the reduction, significant changes are visible in the spectra of all compounds. First, the peak labeled as t_{2g} is shifted to higher energies and split into a doublet. The change originates from the reduction of Fe^{4+} to Fe^{3+} and follows the trend reported by Abbate *et al.* [37]. Simultaneously, the formation of the doublet arises from the splitting of t_{2g} into d_{xz}, d_{yz} and d_{xy} orbitals, respectively, due to the distortion of the unit cell or the formation of oxygen vacancies [40,41]. At the same time, crystal field splitting occurs for the e_g orbitals as well, which split into the d_{z2} and d_{x2-y2} orbitals, respectively. These observations are in line with the formation of a more complex structure of the Ruddlesden-Popper layered perovskite. The splitting is the most intense for the e_g orbital of SFMNb. Moreover, exceptionally this sample gave different spectrum after the re-oxidation. The t_{2g} peak is shifted to higher energies, while e_g peak is significantly less intense. Moreover, the peak originating from Sr 4d – O 2p is shifted to higher energies. It is unlike all other samples in which the aforementioned peak remains almost unaffected in terms of energy regime. This observation is particularly interesting because no significant changes have been observed during XRD, both ex-situ and in-situ high-temperature measurements. The differences in spectra for SFMNb may originate from electron transfer between Fe-Nb or Mo-Nb orbitals.

Figure 5D shows the Fe-$L_{3,2}$ edges of the SFM-based compounds after reduction in H_2. The collected spectra are typical of Fe^{3+} in octahedral coordination [37,42–44]. According to [37] such spectra originate from a high spin $t_{2g}^3e_g^2$ ground state of $3d^5$ and the 10Dq value is calculated to be 1.6 eV. The value was calculated based on the minima of the second derivative of the L_3-edge. The exemplary spectrum with its derivative is plotted in Fig. S5. However, the spectra are characterized by a similar shape, originating from Fe^{3+} cations, and the intensity of the white lines are of different intensity. The intensity of the L-edge carries information about the unoccupied d-orbitals and may suggest a higher valence of the element [45]. In this case, in SFM more Fe^{2+} formed after reduction, compared to both doped materials. The spectra for as-prepared and re-oxidized compounds are presented in Fig. S6 in Supplementary Materials. Regardless of the reduction, the ground state of Fe remained unaffected and iron was found to be present mainly as Fe^{3+} cations.

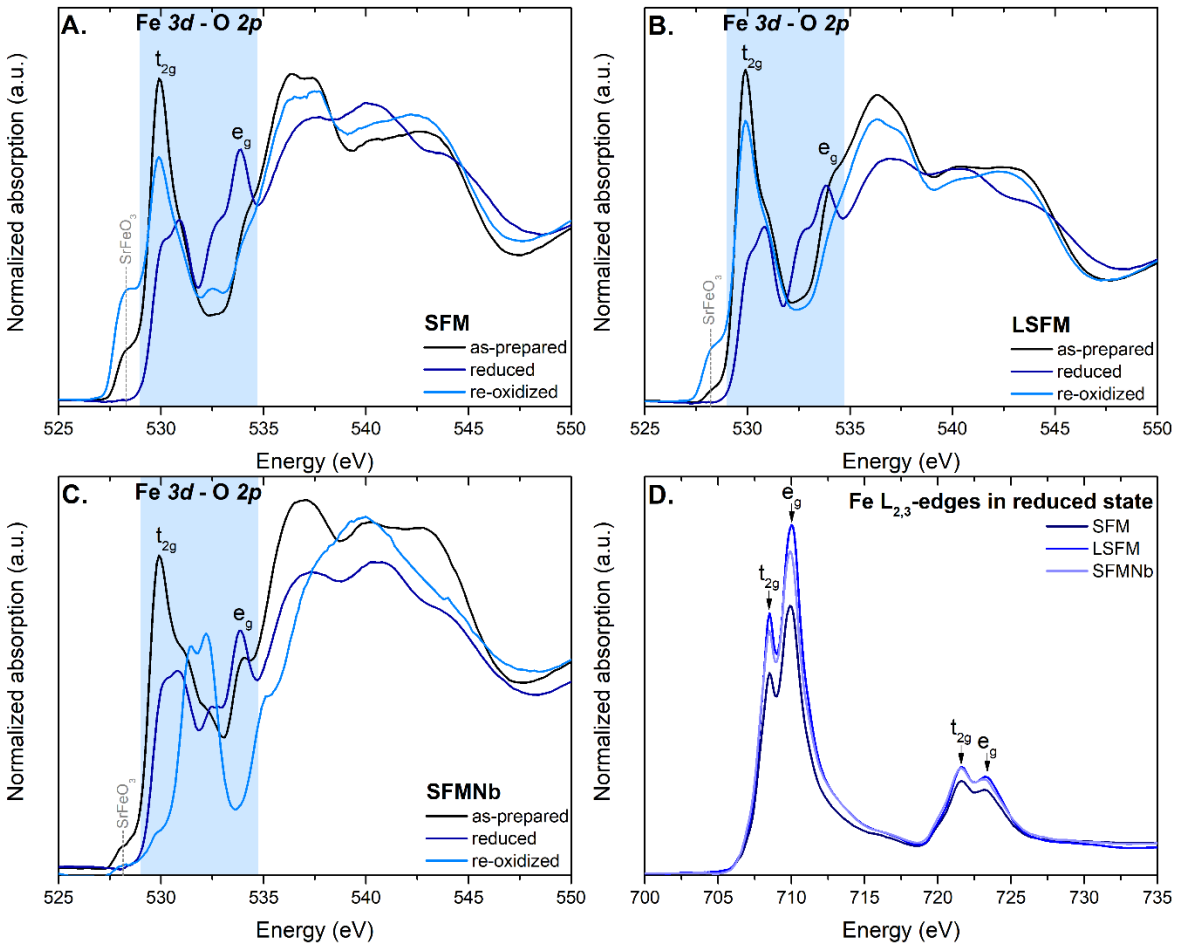

Fig. 5. Normalized X-ray absorption edges collected for compounds in different states (as-prepared, reduced, and re-oxidized): A. O-K edge of SFM, B. O-K edge of LSFM, C. O-K edge of SFMNb, and D. Fe-$L_{3,2}$ edge in reduced state only of all three materials.

The use of hard X-rays allowed to probe the K-edge of iron in the compounds of the interest. Normalized XANES spectra are presented in Figs. 6A-C. As expected, based on the $L_{3,2}$-edges, the K-edge spectra are characteristic of Fe^{3+} in the octahedral coordination of the perovskite [40]. The comparison of the as-prepared SFM spectrum and references is plotted in Fig. S7 in the Supplementary Materials. Although the spectra are of overall similar shape, some significant differences can be spotted. First, the pre-edge feature originating from the presence of hybridized 3d-4p orbitals and two contributions originating from this: dipole transition 1s→4p and quadrupole 1s→3d [46,47]. Hybridization of 3d-4p would not occur in ideal octahedral structures; thus, distortion must be present in SFM-based materials [47].

However, the reduction does not affect the shape of the K-edge, it has an impact on the intensity of the white line. The decrease in white-line intensity is the most visible for doped SFM, suggesting a partial reduction to iron ions as visible in SEM imaging. At the same time, the pre-edge feature was enhanced for the undoped sample. In general, all the analyzed samples have the lowest white line intensity for the reduced samples. This observation coupled with a slight shift of at the pre-edge suggests partial reduction to Fe^{2+} ions. After the re-oxidation process, the white line intensity increased almost back to the original. In the case of both doped SFM-based compounds, the edge got higher, most probably because of the changes in the density of states (DOS). The higher the white line, the lower the DOS is.

The L_3-edges of molybdenum were also measured and normalized spectra are presented in Figs. 6D-F. Based solely on the intensity of the peaks (ratio 3:2), it is easy to confirm that molybdenum is also present in octahedral coordination [48,49]. The first peak at ~2523 eV originates from excitations to the t_{2g} states and the latter peak at ~2527 eV occurs due to the transition to e_g state [29]. Based on Vasala *et al.* [29] in as-prepared samples, both aforementioned states should be empty and the reduction would introduce electrons into the t_{2g} state. As a result, the peak from reduced samples should be lower than in the as-prepared one. Such an observation is made for the pristine SFM and the La-doped one. Interestingly, the behavior for SFMNb is different, which could originate from electron transfer between Mo and Nb cations. Based on L_3 spectra, it may be deduced that molybdenum has been partially reduced to Mo^{5+} during reduction, which can be determined by occupation of the t_{2g} and e_g states. Another indication of octahedral geometry is the value of d-orbital splitting, which was calculated as a difference between two minima in the second derivative of the respective compounds [49]. The second derivatives of the Mo L_3-edge spectra are presented in Fig. 6G-I. The aforementioned splitting were found to be in the range of 4.2 eV – 4.4 eV, typical of the octahedral structure [48,50] and slightly smaller than the other obtained for Mo-based double perovskites [51].

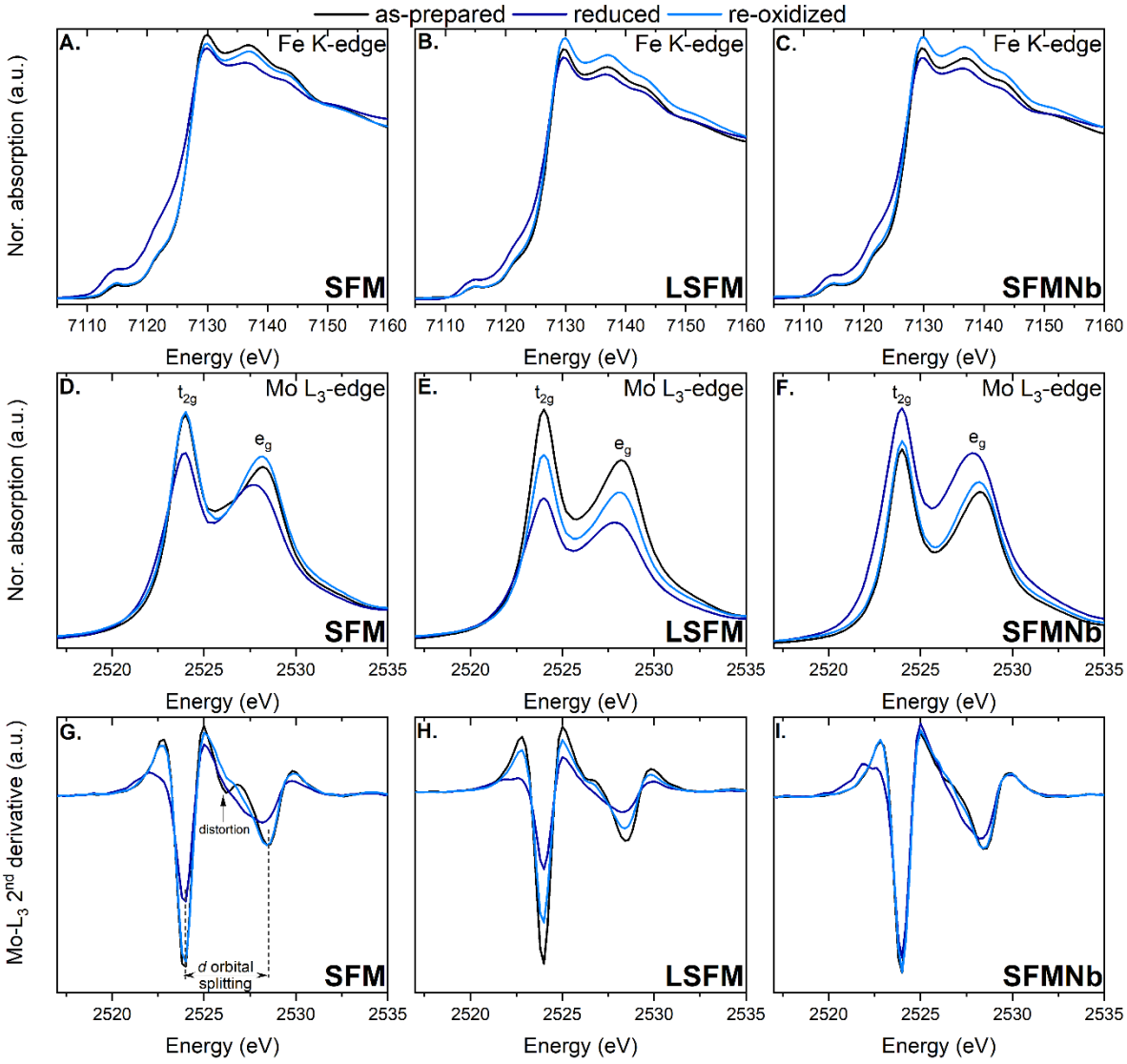

Fig. 6. Normalized Fe-K edges for SFM (A.), LSFM (B.), and SFMNb (C.), normalized Mo L_3-edges for SFM (D.), LSFM (E.), and SFMNb (F.), and 2nd derivative of Mo-L_3 edges: SFM (G.),

LSFM (H.), and SFMNb (I.).

The Fourier Transformed EXAFS spectra of the respective compounds are presented in Fig. 7. Due to the complicated nature of the compounds, only qualitative analysis was performed. The main peak visible at ~1.75 Å in all cases originates from the Fe-O bond. The position of the Fe-O peak corresponds well with the expected bond length from the crystal structures of the prepared compounds. In reduced compounds, the peak is slightly shifted to higher values, which is characteristic of the Ruddlesden-Popper layered perovskite. The re-oxidized materials are characterized by similar bond lengths compared to their as-prepared counterparts, which shows that the structure has been restored to its original state. The next characteristic peak originates from the Fe-Sr bond, which tends to be slightly shorter after the reduction as a result of the formation of the RP phase. Exceptionally for LSFM, this scattering path got elongated, which originates from the expansion of original unit cell during the reduction. The Fe-Sr peak is followed by the peak coming from the single scattering path on Fe-Fe/Mo bonds. In case of Nb-doping, the signal originating from the Fe-Nb scattering pathway would overlap with other Fe-Fe and Fe-Mo paths. As both Fe and Mo occupy equivalent positions, it is impossible to differentiate each contribution to the scattering pathways.

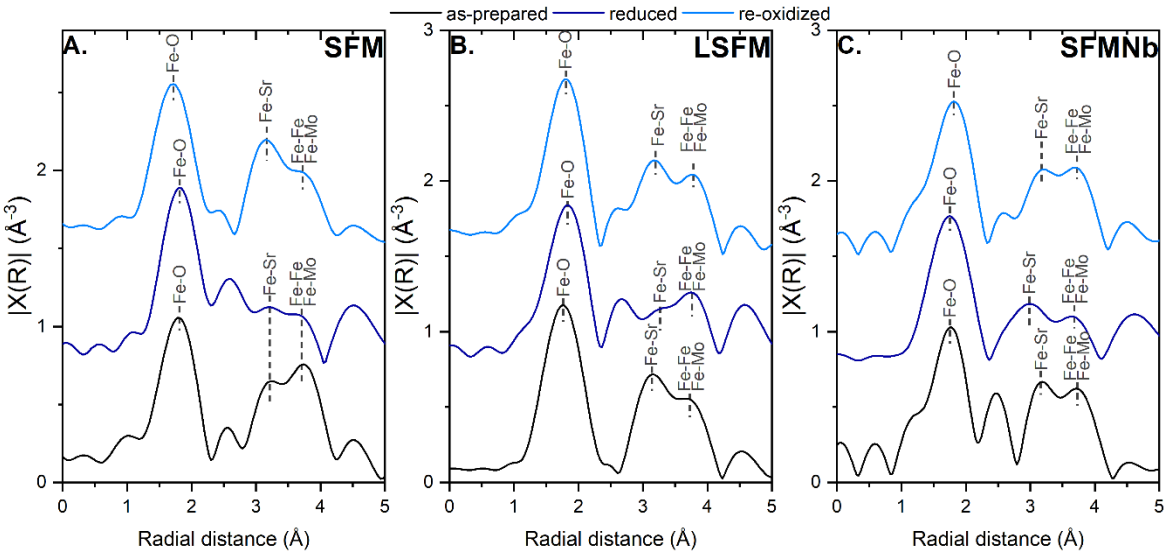

Fig. 7. Fourier Transform of the Fe K-edge EXAFS for: A. SFM, B. LSFM, and C. SFMNb.

As mentioned above, the scattering paths from Fe-Fe and Fe-Mo bonds are overlapping in the Fourier Transformed EXAFS, making it impossible to differentiate between them. Thus, the analysis was extended to wavelet transform to reveal the possible changes during reduction and re-oxidation. The wavelet transform heat maps (not corrected for phase shift) for the LSFM compound in three states are presented in Fig. 8. The area with the highest intensity, visible as red, is characteristic of Fe-O bonds, while the longer bond in the wavevector 6 $Å^{-1}$ originates from interaction with strontium. Both Fe-O and Fe-Sr bonds are well characterized and are in agreement with Fourier Transformed EXAFS. At longer radial distances, two halos formed and allowed to distinguish between iron and molybdenum contributions [50]. It was determined that the halo at approximately 6 $Å^{-1}$ would originate from the Fe-Fe bond [51,52], while the one at 7.5 $Å^{-1}$ would stand for the Fe-Mo bonds, as heavier atoms should contribute to the signal at higher wavevectors [53]. Both bonds with iron and molybdenum are affected by the reduction and re-oxidation processes; however, the one from molybdenum is undergoing more visible elongation and shortening due to redox processes. Interestingly, an additional

signal formed in the reduced LSFM at the wavevector ~4.75 $Å^{-1}$. Despite the same calculation parameters, it is not visible for as-prepared and re-oxidized states, suggesting that it would be linked to the exsolved particles on the perovskite surface.

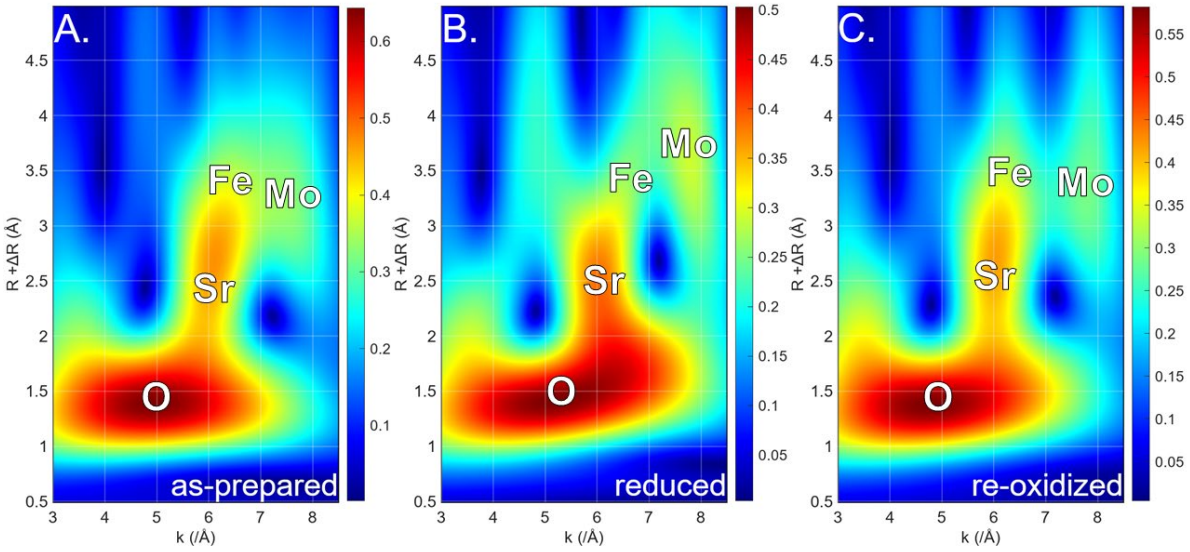

Fig. 8. The EXAFS wavelet transform of LSFM in as-prepared (A.), reduced (B.), and re-oxidized (C.) states.

d. Electrical properties

In order to examine the impact of the La- and Nb-doping on the electrical properties, the direct current 4 wire method was applied. The results of conductivity vs. temperature are plotted in Fig. 9. The three samples in air are characterized by the local maximum of conductivity at 600-650 °C equal to 14.52 S cm^{-1}, 20.20 S cm^{-1}, and 11.03 S cm^{-1} for SFM, LSFM, and SFMNb, respectively. Below the temperature at which the maximum is achieved, all of the compounds are characterized by thermally activated conduction. The conductivity starts to decrease with a temperature above 650 °C. Other groups have observed a similar trend [25,30,54–57]. This behavior is explained by the loss of oxygen from the lattice, which promotes the reduction of iron and/or molybdenum leading to a decrease in the effective charge carrier concentration [30]. At the same time, the formation of oxygen vacancies at higher temperatures would reduce the number of pathways available for the conduction mechanism [15]. According to Niu *et al.* [58] and Yang *et al.* [25] the conduction in SFM-based compounds can be explained as double exchange between Fe 3d-O 2p and Mo 3d-O 2p orbitals. As a result, conduction occurs via the small polaron hopping mechanism through Fe^{2+}/Mo^{6+}-O^{2-}-Fe^{3+}/Mo^{5+} pathways [25,33,56,59].

As hoped, the lanthanum doping has increased the electrical conductivity, but the addition of niobium resulted in lower overall conductivity. At low temperatures, the conductivity of SFMNb is slightly higher than that of the pristine compound. The activation energies were calculated from the Arrhenius formula in the 300-600 ° C range, where linear ln(Tσ) vs. 1/T were observed. The values of calculated E_A for both atmospheres are presented in the Tab. 2. In general, the doping process decreased the activation energy of the conductivity. This decrease could be explained by the increased content of oxygen vacancies [59]. Even the Nb-doped sample, regardless of its negative impact on the conduction, is also characterized by a decrease in E_A.

The conductivity of all compounds in hydrogen has a different behavior: the conductivity gradually increases with temperature throughout the whole temperature range which is in line with the general

behavior [25,30]. Within the conductivity plots two regions can be differentiated: the low-temperature regime up to 500 °C and the high-temperature region located above this threshold value. Different regimes correspond to the change in slope of the conductivity curve. The change is the most prominent for the Nb-doped SFM. The presence of the inflection point in the conductivity curve is a characteristic feature of the small polaron hopping mechanism [56]. Wang *et al.* [59] has explained the presence of two slopes by the existence of two different paths of charge compensation. As a result, two different activation energies must be considered. Calculated values are presented in the Tab. 2. In general, the activation energies are lower in the low-temperature regime. Between 300-500 °C, doping has a positive impact on the activation energy. However, when the high-temperature region is reached, only lanthanum doping is beneficial in terms of activation energy. Similarly to the behavior in air, the LSFM has the highest conductivity in almost the entire temperature range. Only at 800 °C did SFMNb peak with the highest electrical conductivity, whereas at lower temperatures its performance is comparable to undoped SFM. All compounds reached conductivity values at 800 °C equal to 25.52 S cm^{-1}, 31.44 S cm^{-1}, and 34.13 S cm^{-1} for SFM, LSFM, and SFMNb, respectively. The values obtained for air and hydrogen make those double perovskites promising materials for both the anode and cathode in SOC and as a result could possibly be used as electrodes in symmetrical Solid Oxide Cells (sSOFCs) [21]. For example, Zheng et al. [60] studied a similar system $Sr_2Fe_{2-x}W_xO_{6-\delta}$ with an electrical conductivity of ~40 S cm^{-1} as electrodes in quasi-symmetrical setup. The same team has also reported the use of SFM in a symmetrical setup with electrical conductivity of 50 S cm^{-1} in H_2/Ar mixture and 13 S cm^{-1} in air [23]. A similar magnitude of σ were achieved for Cu-doped SFM for use in sSOFCs by Tian et al. [54]. In the work of Niu et al. [58], good electrode performance, stability, and resistance to poisoning were described for $Sr_2TiFe_{1-x}Mo_xO_{6-\delta}$ symmetrical electrodes, even if electrical conductivity in both air and hydrogen did not exceed 2 S cm-1. In light of the aforementioned values, LSFM is undoubtedly worth considering for further studies as electrodes in sSOFC.

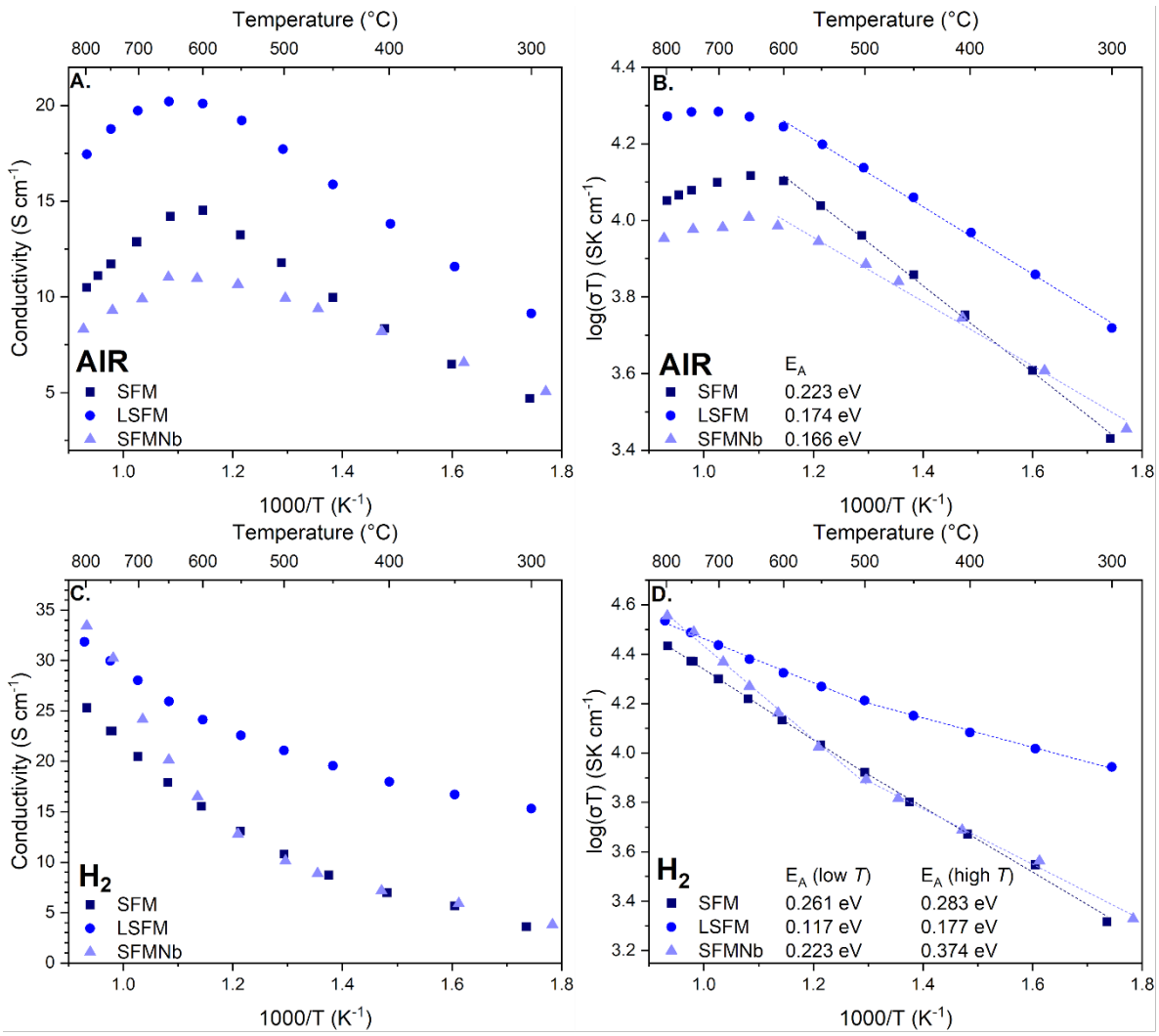

Fig. 9. Electrical conductivities measured in air (A. and B.) and in hydrogen (C. and D.)

Tab. 2. Activation energies calculated from Arrhenius formula for compounds analyzed in air and hydrogen.

	AIR	***H_2***	
	300-550 °C	**300-500 °C**	**500-800 °C**
SFM	**0.223(4) eV**	**0.261(9) eV**	**0.283(1) eV**
LSFM	**0.174(4) eV**	**0.117(4) eV**	**0.177(5) eV**
SFMNb	**0.166(7) eV**	**0.223(9) eV**	**0.374(9) eV**

4. Conclusions

In this work, it was possible to successfully synthesize the double perovskite $Sr_2Fe_{1.5}Mo_{0.5}O_{6-\delta}$ (SFM), as well as its counterparts doped with La and Nb (LSFM and SFMNb, respectively). Although, under

highly reducing atmospheres all three compounds are undergoing the transition to the Ruddlesden-Popper layered perovskite, the La-doping stabilizes the structure, and less new phase was formed. At the same time, exsolution of the Fe-based nanoparticles was observed after the reduction. Moreover, the transition was found to be reversible, and the double perovskite structure could be restored after the re-oxidation. In situ oxidation studies allowed to determine that double perovskite starts with the dissolution of exsolved iron nanoparticles back into the perovskite base at ~250 °C, followed by the incorporation of oxygen up to ~650-700 °C. On the ex-situ XAS measurement, it was found that not only the crystallographic structure is restored to its original but also the local atomic environment can be brought back. As expected, during the reduction, both iron and molybdenum are partially reduced to the lower valence state. The use of wavelet transform on Fe K-edge enabled to distinguish between contributions of Fe-Fe and Fe-Mo bonds in k-space. It was also presented that Fe-Mo bonds are more prone to elongation and shortening during redox processes.

Electrical tests performed in both air and hydrogen proved good electrical conductivity of SFM-based materials in both atmospheres. The most beneficial was the addition of lanthanum as it almost doubled the conductivity in air when compared with the pristine sample. LSFM has also revealed the best conductivity in hydrogen. Taking into account the improvement in conductivity and strongly enhanced stability in reducing atmospheres, the LSFM compound seems to be a promising material for sSOFC.

Conflict of interest

The authors declare that they have no known conflict of interest.

Acknowledgements

The research project was supported by the National Science Center under grant No. NCN 2022/45/N/ST5/02933. This publication was partially developed under the provision of the Polish Ministry and Higher Education project "Support for research and development with the use of research infra-structure of the National Synchrotron Radiation Centre SOLARIS" under contract no 1/SOL/2021/2. We acknowledge SOLARIS Centre for the access to the PIRX and ASTRA beamlines, where the measurements were performed.

Author contributions:

A. Ducka – conceptualization, data curation, formal analysis, investigation, visualization, writing-original draft, writing – review & editing, funding acquisition, project administration;

P. Błaszczak - conceptualization, investigation, writing- original draft, writing – review & editing;

M. Zając – resources, methodology;

A. Maximenko - resources, methodology, supervision, writing – original draft;

M. Gazda - resources, methodology, writing-original draft;

B. Bochentyn - resources, investigation, supervision

Literature

[1] Vasala S, Karppinen M. A2B′B″O6 perovskites: A review. Progress in Solid State Chemistry 2015;43:1–36. https://doi.org/10.1016/j.progsolidstchem.2014.08.001.

[2] Xu X, Zhong Y, Shao Z. Double Perovskites in Catalysis, Electrocatalysis, and Photo(electro)catalysis. Trends Chem 2019;1:410–24. https://doi.org/10.1016/j.trechm.2019.05.006.

[3] Li Y, Chen X, Yang Y, Jiang Y, Xia C. Mixed-Conductor Sr 2 Fe 1.5 Mo 0.5 O 6−δ as Robust Fuel Electrode for Pure CO 2 Reduction in Solid Oxide Electrolysis Cell. ACS Nano 2017;5:11403–12. https://doi.org/10.1021/acssuschemeng.7b02511.

[4] Dong H, Wang M, Liu Y, Han Z. Optimized Solid-State Synthesis of Sr2Fe1.5Mo0.5O6−δ Perovskite: Implications for Efficient Synthesis of Mo-Containing SOFC Electrodes. Crystals (Basel) 2022;12. https://doi.org/10.3390/cryst12111533.

[5] Gou M, Ren R, Sun W, Xu C, Meng X, Wang Z, et al. Nb-doped Sr2Fe1.5Mo0.5O6-δ electrode with enhanced stability and electrochemical performance for symmetrical solid oxide fuel cells. Ceram Int 2019;45:15696–704. https://doi.org/10.1016/j.ceramint.2019.03.130.

[6] Yang X, Chen J, Panthi D, Niu B, Lei L, Yuan Z, et al. Electron doping of Sr2FeMoO6-δ as high performance anode materials for solid oxide fuel cells. J Mater Chem A Mater 2019;7:733–43. https://doi.org/10.1039/c8ta10061f.

[7] Liu Q, Yang C, Dong X, Chen F. Perovskite Sr2Fe1.5Mo0.5O6 as electrode materials for symmetrical solid oxide electrolysis cells. Int J Hydrogen Energy 2010;35:10039–44. https://doi.org/10.1016/j.ijhydene.2010.08.016.

[8] Du Z, Zhao H, Yi S, Xia Q, Gong Y, Zhang Y, et al. High-Performance Anode Material Sr2FeMo0.65Ni0.35O6−δ with In Situ Exsolved Nanoparticle Catalyst. ACS Nano 2016;18:31. https://doi.org/10.1021/acsnano.6b03979.

[9] Li Y, Singh M, Zhuang Z, Jing Y, Li F, Maliutina K. Efficient reversible CO / CO 2 conversion in solid oxide cells with a phase-transformed fuel electrode 2021;64:1114–26.

[10] Wu Y, Li H, Zhang P, Tong S, Han X, Chen H, et al. Multiphase engineering regulation of double perovskite and RP structure heterojunction interfaces for solid oxide fuel cells. Sustainable Materials and Technologies 2024;40:e00905. https://doi.org/10.1016/j.susmat.2024.e00905.

[11] Yang Y, Li W, Yang S, Shen X, Han Z, Yu H, et al. Ni-Substituted Sr2FeMoO6−δ as an Electrode Material for Symmetrical and Reversible Solid-Oxide Cells. ACS Appl Mater Interfaces 2024;16:21790–8. https://doi.org/10.1021/acsami.4c00509.

[12] Lv H, Lin L, Zhang X, Song Y, Matsumoto H, Zeng C, et al. In Situ Investigation of Reversible Exsolution/Dissolution of CoFe Alloy Nanoparticles in a Co-Doped Sr2Fe1.5Mo0.5O6−δ Cathode for CO2 Electrolysis. Advanced Materials 2020;32. https://doi.org/10.1002/ADMA.201906193.

[13] Qiu P, Yang X, Wang W, Wei T, Lu Y, Lin J, et al. Redox-Reversible Electrode Material for Direct Hydrocarbon Solid Oxide Fuel Cells. ACS Appl Mater Interfaces 2020;12:13988–95. https://doi.org/10.1021/acsami.0c00922.

[14] Luo Y, Chang X, Wang J, Zhang D, Fu L, Gu XK, et al. Precise Regulation of In Situ Exsolution Components of Nanoparticles for Constructing Active Interfaces toward Carbon Dioxide Reduction. ACS Nano 2025;19:1463–77. https://doi.org/10.1021/acsnano.4c14279.

[15] Shan P, Ye H, Qian B, Zheng Y, Xiao G. Boosting the catalytic activity of high-order Ruddlesden–Popper perovskite SrEu2Fe2O7-δ air electrode by A-site La doping for CO2 electrolysis in solid oxide electrolysis cells. Fuel 2024;367:131507. https://doi.org/10.1016/j.fuel.2024.131507.

[16] Lv H, Lin L, Zhang X, Song Y, Matsumoto H, Zeng C, et al. In Situ Investigation of Reversible Exsolution/Dissolution of CoFe Alloy Nanoparticles in a Co-Doped Sr2Fe1.5Mo0.5O6−δ Cathode for CO2 Electrolysis. Advanced Materials 2020;32. https://doi.org/10.1002/ADMA.201906193.

[17] Yang Y, Li W, Yang S, Shen X, Han Z, Yu H, et al. Ni-Substituted Sr2FeMoO6−δ as an Electrode Material for Symmetrical and Reversible Solid-Oxide Cells. ACS Appl Mater Interfaces 2024;16:21790–8. https://doi.org/10.1021/acsami.4c00509.

[18] Zhu K, Luo B, Liu Z, Wen X. Recent advances and prospects of symmetrical solid oxide fuel cells. Ceram Int 2022;48:8972–86. https://doi.org/10.1016/J.CERAMINT.2022.01.258.

[19] Tian C, Cheng J, Yang J. A highly active cathode material of Cu-doped Sr2Fe1.5Mo0.5O6 for symmetrical solid oxide fuel cells. Journal of Materials Science: Materials in Electronics 2021;32:1258–64. https://doi.org/10.1007/s10854-020-04898-z.

[20] Liu Q, Dong X, Xiao G, Zhao F, Chen F. A novel electrode material for symmetrical SOFCs. Advanced Materials 2010;22:5478–82. https://doi.org/10.1002/adma.201001044.

[21] Ruiz-Morales JC, Marrero-López D, Canales-Vázquez J, Irvine JTS. Symmetric and reversible solid oxide fuel cells. RSC Adv 2011;1:1403–14. https://doi.org/10.1039/c1ra00284h.

[22] He B, Zhao L, Song S, Liu T, Chen F, Xia C. Sr2Fe1.5Mo0.5O6−δ - Sm0.2Ce0.8O1.9 Composite Anodes for Composite Anodes for Intermediate-Temperature Solid Oxide Fuel Cells Intermediate-Temperature Solid Oxide Fuel Cells. J Electrochem Soc 2012;159:619–26. https://doi.org/10.1149/2.020206jes.

[23] Zheng K, Swierczek K, Polfus JM, Sunding MF, Pishahang M, Norby T. Carbon Deposition and Sulfur Poisoning in SrFe0.75Mo0.25O3-δ and SrFe0.5Mn0.25Mo0.25O3-δ Electrode Materials for Symmetrical SOFCs. J Electrochem Soc 2015;162:1078–87. https://doi.org/10.1149/2.0981509jes.

[24] Mo F, Sm O, Ce O, Wang Y, Liu T, Fang S, et al. Syngas production on a symmetrical solid oxide H 2 O / CO 2 co-. J Power Sources 2016;305:240–8. https://doi.org/10.1016/j.jpowsour.2015.11.097.

[25] Yang X, Chen J, Panthi D, Niu B, Lei L, Yuan Z, et al. Electron doping of Sr2FeMoO6-δ as high performance anode materials for solid oxide fuel cells. J Mater Chem A Mater 2019;7:733–43. https://doi.org/10.1039/c8ta10061f.

[26] Huan Y, Li Y, Yin B, Ding D, Wei T. High conductive and long-term phase stable anode materials for SOFCs: A2FeMoO6 (A = Ca, Sr, Ba). J Power Sources 2017;359:384–90. https://doi.org/10.1016/j.jpowsour.2017.05.079.

[27] Li X, Zhao H, Xu N, Zhou X, Zhang C, Chen N. Electrical conduction behavior of La, Co co-doped SrTiO3 perovskite as anode material for solid oxide fuel cells. Int J Hydrogen Energy 2009;34:6407–14. https://doi.org/10.1016/j.ijhydene.2009.05.079.

[28] Hu X, Qi J, Fu X, Liu J, Qiao S, Gao Y, et al. Conductive origin and design principles of electrically controllable high conductivity La-doped perovskites. J Mater Chem A Mater 2024;12:4019–28. https://doi.org/10.1039/d3ta06845e.

[29] Vasala S, Lehtimäki M, Haw SC, Chen JM, Liu RS, Yamauchi H, et al. Isovalent and aliovalent substitution effects on redox chemistry of Sr2MgMoO6 - δ SOFC-anode material. Solid State Ion 2010;181:754–9. https://doi.org/10.1016/J.SSI.2010.03.037.

[30] Gou M, Ren R, Sun W, Xu C, Meng X, Wang Z, et al. Nb-doped Sr2Fe1.5Mo0.5O6-δ electrode with enhanced stability and electrochemical performance for symmetrical solid oxide fuel cells. Ceram Int 2019;45:15696–704. https://doi.org/10.1016/j.ceramint.2019.03.130.

[31] R.D. S. Revised Effective Ionic Radii and Systematic Studies of Interatomie Distances in Halides and Chaleogenides. Acta Crystallogr 1976;32:751–67. https://doi.org/10.1023/A:1018927109487.

[32] Yu N, Liu T, Chen X, Miao M, Ni M, Wang Y. Co-generation of liquid chemicals and electricity over Co-Fe alloy/perovskite anode catalyst in a propane fueled solid oxide fuel cell. Sep Purif Technol 2022;291. https://doi.org/10.1016/j.seppur.2022.120890.

[33] Xi X, Cao ZS, Shen XQ, Lu Y, Li J, Luo JL, et al. In situ embedding of CoFe nanocatalysts into Sr3FeMoO7 matrix as high-performance anode materials for solid oxide fuel cells. J Power Sources 2020;459. https://doi.org/10.1016/j.jpowsour.2020.228071.

[34] Liu Q, Dong X, Xiao G, Zhao F, Chen F. A novel electrode material for symmetrical SOFCs. Advanced Materials 2010;22:5478–82. https://doi.org/10.1002/adma.201001044.

[35] Awasthi A, Bhatt YJ, Krishnamurthy N, Ueda Y, Garg SP. The reduction of niobium and tantalum pentoxides by silicon in vacuum. vol. 315. 2001.

[36] Suntivich J, Hong WT, Lee YL, Rondinelli JM, Yang W, Goodenough JB, et al. Estimating hybridization of transition metal and oxygen states in perovskites from o k -edge X-ray absorption spectroscopy. Journal of Physical Chemistry C 2014;118:1856–63. https://doi.org/10.1021/jp410644j.

[37] Abbate M, De Groot FMF, Fuggle JC, Fujimori A, Strebel O, Lopez MF, et al. Controlled-valence properties of La1-xSrxFeO3 and La1-xSrxMnO3 studied by soft-x-ray absorption spectroscopy. Phys Rev B 1992;46:4511–9. https://doi.org/10.1103/PhysRevB.46.4511.

[38] Wu Z, Benfatto M, Pedio M, Cimino R, Mobilio S, Barman S, et al. Theoretical analysis of x-ray-absorption near-edge fine structure at the O and metal edges of LaFe and LaCo. Phys Rev B Condens Matter Mater Phys 1997;56:2228–33. https://doi.org/10.1103/PhysRevB.56.2228.

[39] Frati F, Hunault MOJY, De Groot FMF. Oxygen K-edge X-ray Absorption Spectra. Chem Rev 2020;120:4056–110. https://doi.org/10.1021/acs.chemrev.9b00439.

[40] Xi XA, Liu JW, Luo WZ, Fan Y, Zhang JJ, Luo J-LJ-LL, et al. Unraveling the Enhanced Kinetics of Sr2Fe1+xMo1-xO6-δ Electrocatalysts for High-Performance Solid Oxide Cells. Adv Energy Mater 2021;11:1–10. https://doi.org/10.1002/aenm.202102845.

[41] Liao Y, Xi X, Chen H, Liu J, Fu XZ, Luo JL. The emerging Sr2FeMoO6-based electrocatalysts for solid oxide electrochemical cell: synthesis, modulation and applications. Chemical Synthesis 2024;4. https://doi.org/10.20517/cs.2023.47.

[42] Sun H, Xu X, Hu Z, Tjeng LH, Zhao J, Zhang Q, et al. Boosting the oxygen evolution reaction activity of a perovskite through introducing multi-element synergy and building an ordered structure. J Mater Chem A Mater 2019;7:9924–32. https://doi.org/10.1039/c9ta01404g.

[43] Kuiper P, Searle BG, Rudolf P, Tjeng LH, Chen CT. X-ray magnetic dichroism of antiferromagnet Fe2O3: The orientation of magnetic moments observed by Fe 2p x-ray absorption spectroscopy. Phys Rev Lett 1993;70:1549–52. https://doi.org/10.1103/PhysRevLett.70.1549.

[44] Kuo CY, Hu Z, Yang JC, Liao SC, Huang YL, Vasudevan RK, et al. Single-domain multiferroic BiFeO3 films. Nat Commun 2016;7:1–7. https://doi.org/10.1038/ncomms12712.

[45] Baker ML, Mara MW, Yan JJ, Hodgson KO, Hedman B, Solomon EI. K- and L-edge X-ray absorption spectroscopy (XAS) and resonant inelastic X-ray scattering (RIXS) determination of differential orbital covalency (DOC) of transition metal sites. Coord Chem Rev 2017;345:182–208. https://doi.org/10.1016/j.ccr.2017.02.004.

[46] Westre TE, Kennepohl P, DeWitt JG, Hedman B, Hodgson KO, Solomon EI. A multiplet analysis of Fe K-edge 1s → 3d pre-Edge features of iron complexes. J Am Chem Soc 1997;119:6297–314. https://doi.org/10.1021/ja964352a.

[47] Yamamoto T. Assignment of pre-edge peaks in K-edge x-ray absorption spectra of 3d transition metal compounds: electric dipole or quadrupole? X-Ray Spectrometry 2008;37:572–84. https://doi.org/10.1002/xrs.1103.

[48] Freitas AP, André RF, Poucin C, Le TKC, Imbao J, Lassalle-Kaiser B, et al. Guidelines for the Molybdenum Oxidation State and Geometry from X-ray Absorption Spectroscopy at the Mo L2,3-Edges. Journal of Physical Chemistry C 2021;125:17761–73. https://doi.org/10.1021/acs.jpcc.1c01875.

[49] Aritani H, Tanaka T, Funabiki T, Yoshida S, Eda K, Sotani N, et al. Study of the local structure of molybdenum-magnesium binary oxides by means of Mo L3-edge XANES and UV-vis spectroscopy. Journal of Physical Chemistry 1996;100:19495–501. https://doi.org/10.1021/jp9615464.

[50] Iglesias-Juez A, Chiarello GL, Patience GS, Guerrero-Pérez MO. Experimental methods in chemical engineering: X-ray absorption spectroscopy—XAS, XANES, EXAFS. Canadian Journal of Chemical Engineering 2022;100:3–22. https://doi.org/10.1002/cjce.24291.

[51] Li D, Li H, Wen Q, Gao C, Song F, Zhou J. Investigation on Photo-Assisted Fenton-like Mechanism of Single-Atom Mn–N–Fe–N–Ni Charge Transfer Bridge Across Six-Membered Cavity of Graphitic Carbon Nitride. Adv Funct Mater 2024;34:1–14. https://doi.org/10.1002/adfm.202313631.

[52] Zhu L, Li Z, Yang M, Zhou Y, Chen J, Xie F, et al. An Effective Approach to Enhance Hydrogen Evolution Reaction and Hydrogen Oxidation Reaction by Ni Doping to MoO3. Small 2023;19:1–8. https://doi.org/10.1002/smll.202303481.

[53] Muñoz M, Farges F, Argoul P. Continuous Cauchy wavelet transform of XAFS spectra. Physica Scripta T 2005;T115:221–2. https://doi.org/10.1238/Physica.Topical.115a00221.

[54] Tian C, Cheng J, Yang J. A highly active cathode material of Cu-doped Sr2Fe1.5Mo0.5O6 for symmetrical solid oxide fuel cells. Journal of Materials Science: Materials in Electronics 2021;32:1258–64. https://doi.org/10.1007/s10854-020-04898-z.

[55] Chen L, Xu J, Wang X, Xie K. Sr2Fe1.5+xMo0.5O6 cathode with exsolved Fe nanoparticles for enhanced CO2 electrolysis. Int J Hydrogen Energy 2020;45:2–8. https://doi.org/10.1016/j.ijhydene.2020.02.140.

[56] Rath MK, Lee KT. Superior electrochemical performance of non-precious Co-Ni-Mo alloy catalyst-impregnated Sr2FeMoO6-δ as an electrode material for symmetric solid oxide fuel cells. Electrochim Acta 2016;212:678–85. https://doi.org/10.1016/j.electacta.2016.07.037.

[57] Wu Y, Li H, Zhang P, Tong S, Han X, Chen H, et al. Multiphase engineering regulation of double perovskite and RP structure heterojunction interfaces for solid oxide fuel cells. Sustainable Materials and Technologies 2024;40:e00905. https://doi.org/10.1016/j.susmat.2024.e00905.

[58] Niu B, Jin F, Zhang L, Shen P, He T. Performance of double perovskite symmetrical electrode materials Sr2TiFe1–xMoxO6–δ (x = 0.1, 0.2) for solid oxide fuel cells. Electrochim Acta 2018;263:217–27. https://doi.org/10.1016/J.ELECTACTA.2018.01.062.

[59] Wang Y, Lei X, Zhang Y, Chen F, Liu T. In-situ growth of metallic nanoparticles on perovskite parent as a hydrogen electrode for solid oxide cells. J Power Sources 2018;405:114–23. https://doi.org/10.1016/J.JPOWSOUR.2018.10.023.

[60] Zheng K, Lach J, Czaja P, Gogacz M, Czach P, Brzoza-Kos A, et al. Designing high-performance quasi-symmetrical solid oxide cells with a facile chemical modification strategy for Sr2Fe2−xWxO6−δ ferrites electrodes with in situ exsolution of nanoparticles. J Power Sources 2023;587. https://doi.org/10.1016/j.jpowsour.2023.233707.